ACS OMEGA

Open Access

http://pubs.acs.org/journal/acsodf

Article

Simultaneous Second Harmonic Generation and Multiphoton Excited Photoluminescence in Samarium-Doped $BaTiO_3$ Nanoparticles Functionalized with Poly(ethylene glycol)

Sandra Fuentes,* Duxan Arancibia, Marcelo Rojas, Francisca Carmona, Andrea Ortega, Julio Valenzuela, Christian Hernández-Álvarez, and Inocencio R. Martín*

Cite This: *ACS Omega* 2024, 9, 28061−28071

Read Online

ACCESS | Metrics & More | Article Recommendations

ABSTRACT: In this work, samarium-doped $BaTiO_3$ (BT:Sm) nanoparticles (NPs) were prepared and coated with poly(ethylene glycol) (PEG) to investigate their optical characteristics and compatibility with biological systems. The structure, particle morphology, optical properties, and biological compatibility of the NPs were assessed. The results demonstrated the formation of BT:Sm and [(BT:Sm)-PEG]. The relative intensities and positions of peaks in the X-ray diffraction (XRD) are consistent with an average crystallite size of ∼75 nm. The Raman spectra showed that Sm doping produced the typical tetragonal peaks at around 306 and 715 cm^{-1}, and Fourier transform infrared (FTIR) spectroscopy showed that the PEGylation process was effective. Also, our investigation demonstrates the potential of these NPs as very temperature-sensitive nanosensors with a resolution exceeding 0.5 °C, which is achievable through optical excitation. We also analyze their emission properties. Finally, we present a study related with the mitochondrial activity of naked and PEG-coated NPs. The results indicate that neither naked nor PEG-coated NPs exhibit changes in mitochondrial metabolism, as indicated by quantitative cell viability and morphological visualization. The PEG-coated NPs prevented the formation of aggregates in cell culture compared to naked NPs, demonstrating the significance of PEG as a stabilizing agent.

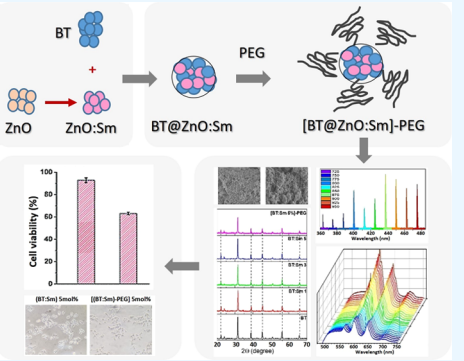

1. INTRODUCTION

Recent years have witnessed extraordinary advancements in nanomaterials, with a growing emphasis on developing multifunctional nanoparticles (NPs) with tailored properties for various applications.[1] Due to their unique optical properties, high photostability, broad transparency ranges in the visible and near-infrared regions, and potential in nonlinear optical devices, doped $BaTiO_3$ nanoparticles (BT-NPs) have attracted considerable interest among these nanomaterials.[2] $BaTiO_3$, a well-known ferroelectric material with high second-order nonlinear susceptibility, enables efficient second harmonic generation (SHG), generating coherent light at exactly half the excitation wavelength.[3−5] In addition, BT-NPs can undergo multiphoton excited photoluminescence (MP-PL), which occurs when multiple photons are absorbed simultaneously, resulting in the emission of photons with higher energy.[6,7] These phenomena are essential for several optical applications.

On the other hand, owing to the unique 4fn inner shell configurations of Lanthanide (Ln) ions, Ln-doped nanomaterials can perform ultrasensitive in vitro and in vivo bioassays with excellent photostability, narrow emission bands, and high chemical stability based on their enhanced magnetic and optical properties.[8] The optical properties of Ln elements critically depend on the lattice of the host with specific symmetry in which the ions reside. Thus, it is essential to seek suitable host matrices to achieve the desired luminescence.[9] Besides, the cation incorporation strategy has also been demonstrated to effectively manipulate the microstructure of Ln ions containing near-infrared (NIR)-II luminescent NPs to improve their optical performance.[10]

Lanthanide-doped nanomaterials play a key role in biomedical applications and are categorized into three types of transitions:[11] (a) Stokes visible emission under ultraviolet (UV) excitation, typically <400 nm excitation, for Eu^{3+} (630 nm), Tb^{3+} (540 nm), Sm^{3+} (650 nm) and Dy^{3+} (570 nm). (b) Stokes emission in NIR (λ > 1 μm), where most Ln atoms demonstrate Stokes emission with obviously higher quantum efficiency than the up-conversion processes. The most prominent rare-earth ions for in vivo NIR imaging are Nd^{3+}

Received: January 31, 2024
Revised: May 17, 2024
Accepted: June 6, 2024
Published: June 17, 2024

(emission at 860, 1060, and 1330 nm), Er^{3+} (emission at 1530 nm), and Ho^{3+} (emission at 1450 nm). (c) Anti-stokes (up-conversion) emission under NIR photoexcitation (typically 980 nm excitation for Yb^{3+} sensitizers or 808 nm photo-excitation for Nd^{3+} sensitizers) is used to achieve visible and multicolor emission from activators such as Tm^{3+}, Er^{3+}, Ho^{3+}, and Tb^{3+}.[12,1312,13] Biomedical applications in NIR-activatable NPs may offer deeper light penetration owing to less extensive scattering and absorption by endogenous chromophores in the NIR spectral region.[14,15]

NPs have emerged as promising tools for biomedical research and applications. However, the interaction of NPs with biological systems is a crucial factor that must be thoroughly understood for safe and effective use in biomedical applications.[16] Improving NPs stability, dispersibility, and biocompatibility depends on modifying their surface with biocompatible materials.[17] Poly(ethylene glycol) (PEG) functionalization has been extensively used to enhance further the dispersibility and stability of BT-NPs in various solvents.[18−20] PEG is a hydrophilic polymer well-known for its biocompatibility and resistance to protein adsorption, opsonization, and immune system recognition.[21,22] The functionalization of NPs with PEG has been shown to increase their colloidal stability, decrease their aggregation propensity, and increase their circulation time in biological environments.[23] In addition, PEG functionalization permits the incorporation of additional functionalities, such as targeting ligands or surface modifications, to endow NPs with specific properties.[24] These characteristics make PEG-coated NPs appealing for numerous biomedical applications, including drug delivery, imaging, and tissue engineering.[25,26] The biocompatibility of PEG-coated NPs has been thoroughly investigated in cell culture studies, which is crucial in determining their potential for in vivo applications. Cell culture models offer invaluable insights into the cellular responses and interactions of NPs, allowing for the evaluation of their cytotoxicity, cellular uptake, and intracellular fate.[27−29] These studies clarify the safety and efficacy of PEG-coated NPs in interactions with biological systems.

The present study explores the concurrent manifestations of SHG and MP-PL within (PEG)-coated BT-NPs. We present a comprehensive examination of the synthesis, morphology, and biological compatibility of naked BT:Sm and PEG-coated BT:Sm NPs, aiming to engineer materials that offer optimal optical characteristics and biological compatibility for their application as contrast agents.

2. EXPERIMENTAL SECTION

2.1. Materials. Tetrabutyl titanate (TBT, 97%), barium chloride ($BaCl_2$, 99.999%), samarium(III) chloride ($SmCl_3$, 99.9%), sodium hydroxide (NaOH, ≥98%), and poly(ethylene glycol) ($(HO(CH_2CH_2O)_nH)$, MW = 4000) were purchased from Sigma−Aldrich as starting materials.

2.2. Synthesis of BT:Sm NPs. $BaTi_{(1-x)}O_3$:Sm_x NPs (BT:Sm) with x = 0, 1, 3, and 5 mol % Sm as their nominal dopant ion concentration, were synthesized by sol−sol−gel-hydrothermal process was used with tetrabutyl titanate (TBT), barium chloride ($BaCl_2$), and samarium(III) chloride ($SmCl_3$) as starting materials. First, an aqueous solution was prepared by dissolving $BaCl_2$ in 4 mL of deionized water, and another solution was prepared by dissolving $SmCl_3$ in 2 mL of deionized water. Then, 1 mL of TBT was diluted with 8.2 mL of ethanol for 10 min to form a white solution, which was added dropwise over 3 h with stirring at 60 °C to a previously prepared solution of $BaCl_2$ and $SmCl_3$.

NaOH was added while stirring with N_2 bubbling through the solution, and a white homogeneous colloidal barium samarium titanium slurry was formed. A 100 mL Teflon-lined stainless-steel reactor was used to hold the mixed solution. It was sealed and heated for 24 h at 180 °C. After the reaction, the autoclave was allowed to cool to ambient temperature. The as-prepared white powder that adhered to the Teflon container's inner wall and bottom was collected, centrifuged, and washed with ethanol and distilled water to remove any leftover ions before drying at 60 °C for 6 h.[30]

2.3. Synthesis of PEG-Coated BT:Sm, [(BT:Sm)-PEG] NPs. PEG was dissolved in deionized water, and an aqueous suspension was obtained. The resulting solution was filtered through coarse- and fine-fritted funnels in succession. Then, it was successively microfiltered using a Millipore system with 3.0 and 0.45 μm membranes. [(BT:Sm)-PEG] NPs were prepared (BT:Sm was 4 wt % of the PEG). Subsequently, these solutions were transferred to a 100 mL flask and placed in an ultrasonic reactor. On six separate occasions, vibrations were produced with an ultrasonic cleaner to sonicate the solutions for 50 s at a frequency of ∼40 kHz and a power of 50 W. The suspension was centrifuged for 10 min to separate the solid from the solution. The precipitate was washed with a deionized water resin (DI) and dried at 70 °C for 24 h.

2.4. Characterization of Nanoparticles. X-ray diffraction (XRD) data were acquired using a Siemens Advanced D-8 diffractometer with Cu Kα radiation at 40 kV and 30 mA. The morphology of each sample was examined using a field emission scanning electron microscope (SEM), Hitachi model SU5000, equipped with an energy-dispersive X-ray spectroscopy (EDX) detector. Raman spectra were recorded on a Witec model CRC200 using a 5.5 mW laser with a wavelength of 633 nm of a He:Ne laser line. Fourier transform infrared (FTIR) spectroscopy measurements were performed by using a PerkinElmer Frontier MIR/FIR apparatus. The hydrodynamic radius and zeta potential measurements of the particles were determined by dynamic light scattering by means of a Malvern Zetasizer NanoZS 90 (Malvern Instruments, U.K.).

Emission spectra were measured using an Andor Shamrock 303i spectrometer with a silicon iDus CCD camera detector and were corrected for apparatus response. An excitation source was used as a tunable EKSPLA/NT342/3/UVE 10 ns pulsed laser (optical parametric oscillator—OPO) with a repetition rate of 10 Hz and a continuous DPSS laser at 473 nm. Luminescence decay curves were recorded using a 200 MHz LeCroy WS424 oscilloscope and a photomultiplier tube (PMT)-Hamamatsu R928.

2.5. Hydrodynamic Radius and ζ Potential Measurements. Measurements were performed in the pH range between 3.0 and 10.0 in order to identify the point of maximum dispersion. Sample conditions were 1 mg of nanoparticles per mL of buffer solution. Prior to the measurements, the nanoparticles were resuspended by applying ultrasound in three cycles of 30 s and 50% of the maximum capacity of the UP200 St tip sonicator (Hielscher, Germany).

2.6. Cell Culture and Exposure of Nanoparticles. Human embryonic kidney (HEK293-T) cells were grown in Dulbecco's modified Eagle's medium (DMEM, Gibco), supplemented with 10% (v/v) fetal bovine serum (Gibco),

https://doi.org/10.1021/acsomega.4c00974
ACS Omega 2024, 9, 28061−28071

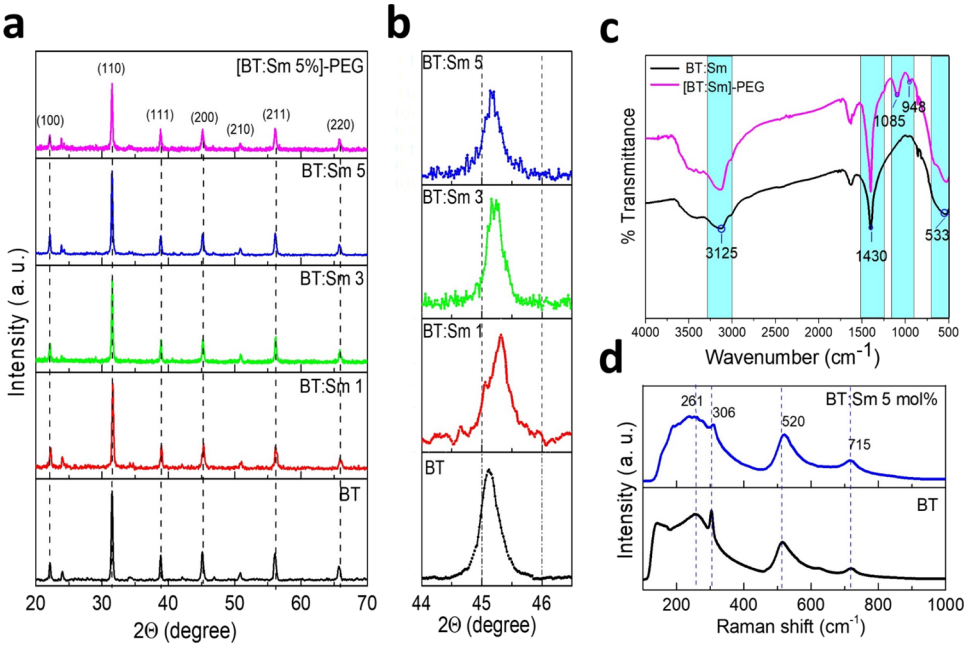

Figure 1. XRD patterns of BT and BT:Sm (a, b); FTIR spectra BT:Sm and [(BT:Sm)-PEG] 5 mol % (c); Raman spectra BT and BT:Sm 5 mol % (d).

100 U/mL penicillin (Gibco), and 100 μg/mL streptomycin (Gibco) at 37 °C with 5% CO_2. The cells were seeded in 96-well plates at a density of 2 × 104 cells/mL for the experiments involving NPs and incubated overnight. The following day, the culture medium was replaced with a new medium containing 1% FBS and various concentrations of NPs (0, 3.125, 6.25, 12.5, 25, 50, 100, and 200 μg/mL). The cells were incubated with NPs for 24 h. The NPs were resuspended in a culture medium, diluted to desired concentrations, and then sonicated in a sonicator bath at room temperature for 5 min to prevent NPs aggregation before cell exposure. Cells without NPs exposure served as the control conditions in each experiment.

2.7. Cell Viability Study. The water-soluble Tetrazolium 1 (WST-1) assay was used to determine possible naked or [(BT:Sm)-PEG] NPs-induced cell death. Briefly, cells were seeded in 96-well plates in culture media and allowed to attach overnight. The following day, cells were treated with various concentrations of NPs at 37 °C in a humidified atmosphere of 5% CO_2/95% air for 24 h. After the indicated incubation time, 20 μL of WST-1 was added to each well. After 3 h of incubation, the plate with the cells was read at 450 nm in a microplate reader (Fermelo). The cell viability (mitochondrial activity) is expressed as the percentage of absorbance compared to the control.

2.8. Cell Morphology Visualization. Images were captured utilizing an Olympus BX60 Light-field microscope outfitted with a 20 x Olympus UplanFI objective and a Leica DFC450 C camera.

2.9. Statistical Data Analysis. GraphPad Prism 8 was utilized for statistical analysis (GraphPad Software, Inc., San Diego, CA). All the data were expressed as mean ± SD, and one-way ANOVA (analysis of variance) followed by Dunnett's test was used for the statistical analysis using GraphPad software (GraphPad Software, Inc., San Diego, CA).

3. RESULTS AND DISCUSSION

3.1. Physicochemical Characterization of BT:Sm NPs. XRD patterns for BT-NPs doped with Sm^{3+} ions (BT:Sm) and the (BT:Sm)-PEG 5 mol % sample are shown in Figure 1a, where BT, BT:Sm, and [(BT:Sm)-PEG] 5 mol % were analyzed. Seven characteristic peaks around 22, 31, 39, 45, 51, 56, and 66 in the 2θ region, which correspond to the (100), (110), (111), (200), (210), (211,) and (220) planes, were observed for all the samples. The peaks can be indexed as the cubic lattice (space group $Pm3m$) of BT, and the calculated lattice constants are consistent with the CPDS card No. 31−0174 without other secondary phases related to $BaCO_3$ or samarium oxide. This result indicates that the Sm ions were homogeneously incorporated into the BT lattice. Figure 1b shows the magnified (002) and (200) peaks near 2θ = 45°. Also, a solitary diffraction peak at (200) indicates that the particles maintain stability in their cubic structure at ambient temperature, consistent with our previously reported findings.[31]

The crystallite size was estimated from the BT (110) reflection as measured by XRD and using the Debye−Scherer equation, which is given as $d = k\lambda/[\beta/\cos(\theta)]$, where d is the size of crystallite, $k \sim 1$ is the shape factor, λ = 0.1540 nm is the wavelength of the Cu Kα radiation, β is the full width at half-maximum (fwhm), and θ is the diffraction angle. The average crystallite sizes of the BT, BT:Sm1, BT:Sm3, BT:Sm5, and [(BT:Sm)-PEG] 5 mol % samples were ∼53, ∼64, ∼69, ∼72, and ∼75 nm, respectively. The FTIR spectra of BT:Sm and [(BT:Sm)-PEG] 5 mol % are shown in Figure 1c. The peak at about 3423 cm^{-1} corresponds to the stretching of the bonded O−H group. The broad bands between the wavelengths 600−400 cm^{-1} (533 cm^{-1}) correspond to the bending of the Ti−O bonds of BT, which agree with the signals expected for these NPs.[32] The signal at ∼1085 cm^{-1}, corresponding to the C−O−C signal of PEG, is within the expected range for aliphatic ethers (1150−1085 cm^{-1}), and the absorption peak at 950 cm^{-1} is due to the out-of-plane bending

https://doi.org/10.1021/acsomega.4c00974
ACS Omega 2024, 9, 28061−28071

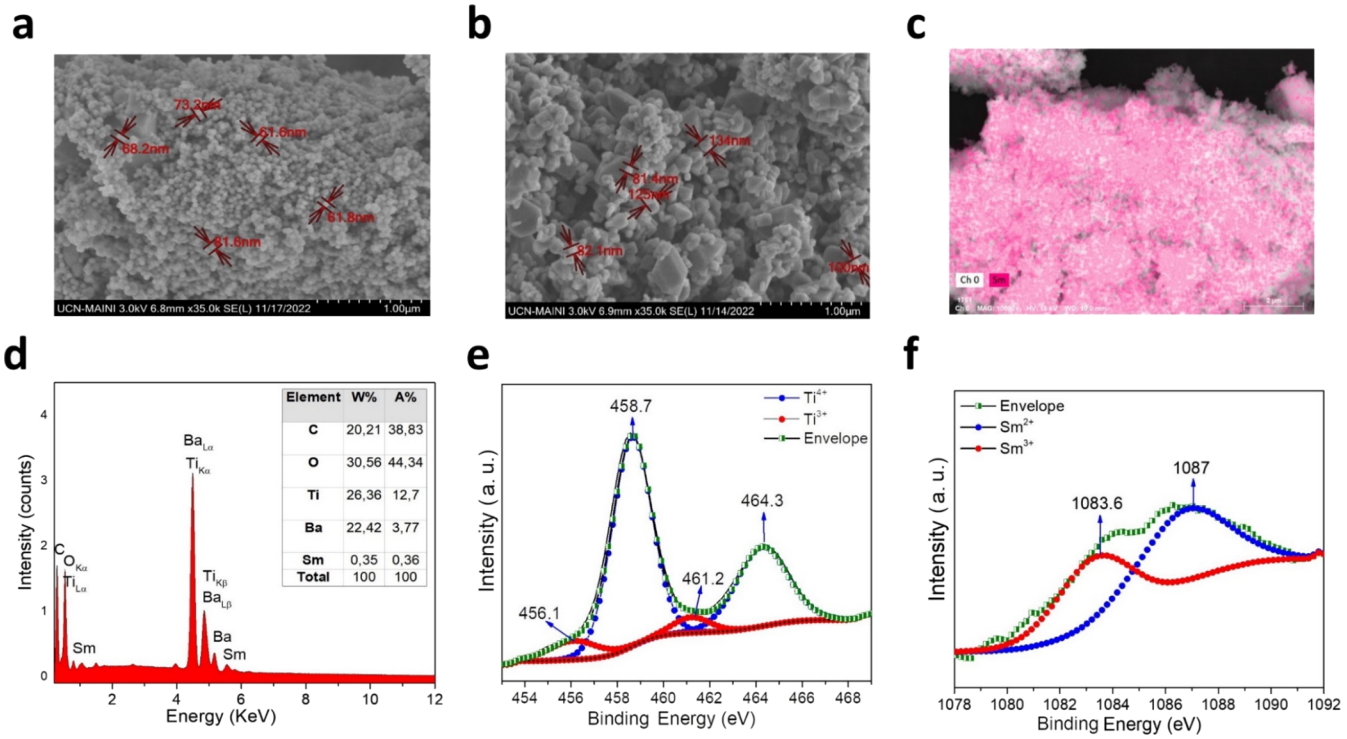

Figure 2. SEM patterns BT:Sm and [(BT:Sm)-PEG] 5 mol % (a, b); elemental map BT:Sm 5 mol %; (c) EDS analysis BT:Sm 5 mol % (d); Ti 2p (e) and Sm 3d (f) XPS spectra of BT:Sm 5 mol %.

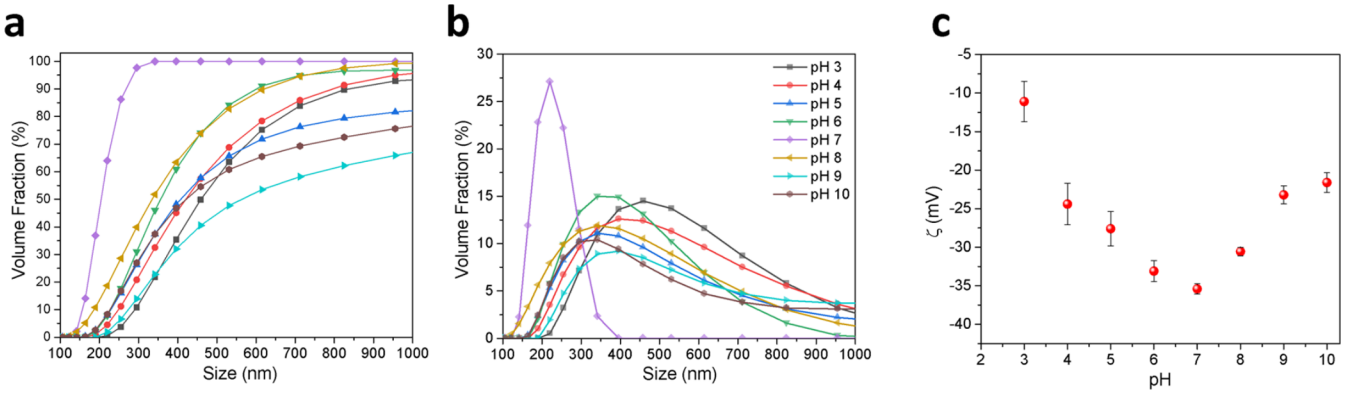

Figure 3. pH effect on Size distribution: (a) accumulate volume fraction; (b) frequency; and (c) ζ potential measurements of [(BT:Sm)-PEG] 5 mol % NPs.

vibration of −CH, present in the polymer that is being used as a coating agent.[32]

The spectra of BT show broad peaks at 261, 306, 520, and 715 cm^{-1}, which correspond to A1 [E(TO)], B1 [E(TO + TO)], A1 [E(TO)], and [E(LO)] modes, respectively (Figure 1d). The strong Raman peaks near 306 and 715 cm^{-1} correspond to the tetragonal BT phase (4 mm symmetry), and the peak at 520 cm^{-1} is attributed to BT cubic symmetry, as determined by XRD analysis in the BT and BT:Sm 5 mol %.[33] At 181 cm^{-1}, an antiresonance effect was found as an interference feature between the sharp A1(TO1) and the broad A1(TO1) modes (TO_2) present only in the BT-NPs. Busca et al. reported a distortion of the TiO_6 octahedron in the cubic BT phase, inducing a pseudo tetragonality of the cubic phase, where both phases (cubic and tetragonal) of the BT coexist in different percentages.[34] Finally, the tetragonal structure of the BT and BT:Sm NPs is confirmed by the Raman spectra of the samples. However, Sm doping causes the typical tetragonal peaks around 306 and 715 cm^{-1} to be less intense than in undoped BT-NPs.

The morphology was determined by using SEM micrograph images of the samples. The BT:Sm 5 mol % image shows uniform small spherical aggregates in clusters of different sizes and uniform dispersion of particles with an average particle size of 60 nm (Figure 2a). The image of [(BT:Sm)-PEG] 5 mol % shows agglomeration of spherical aggregates fuse, with an average particle size of 130 nm (Figure 2b). The increase in particle size with PEG can be explained by the polymer in the sample fusing the particles and increasing the particle size.

The elemental map (EM) of the BT:Sm NPs shows the distribution of Sm (III) across the surface of the sample (Figure 2c). EDS analysis of the same sample showed only the presence of Ba, Ti, O, and Sm, without indicating any other contamination, as seen in the weight and atomic percentages of

https://doi.org/10.1021/acsomega.4c00974
ACS Omega 2024, 9, 28061−28071

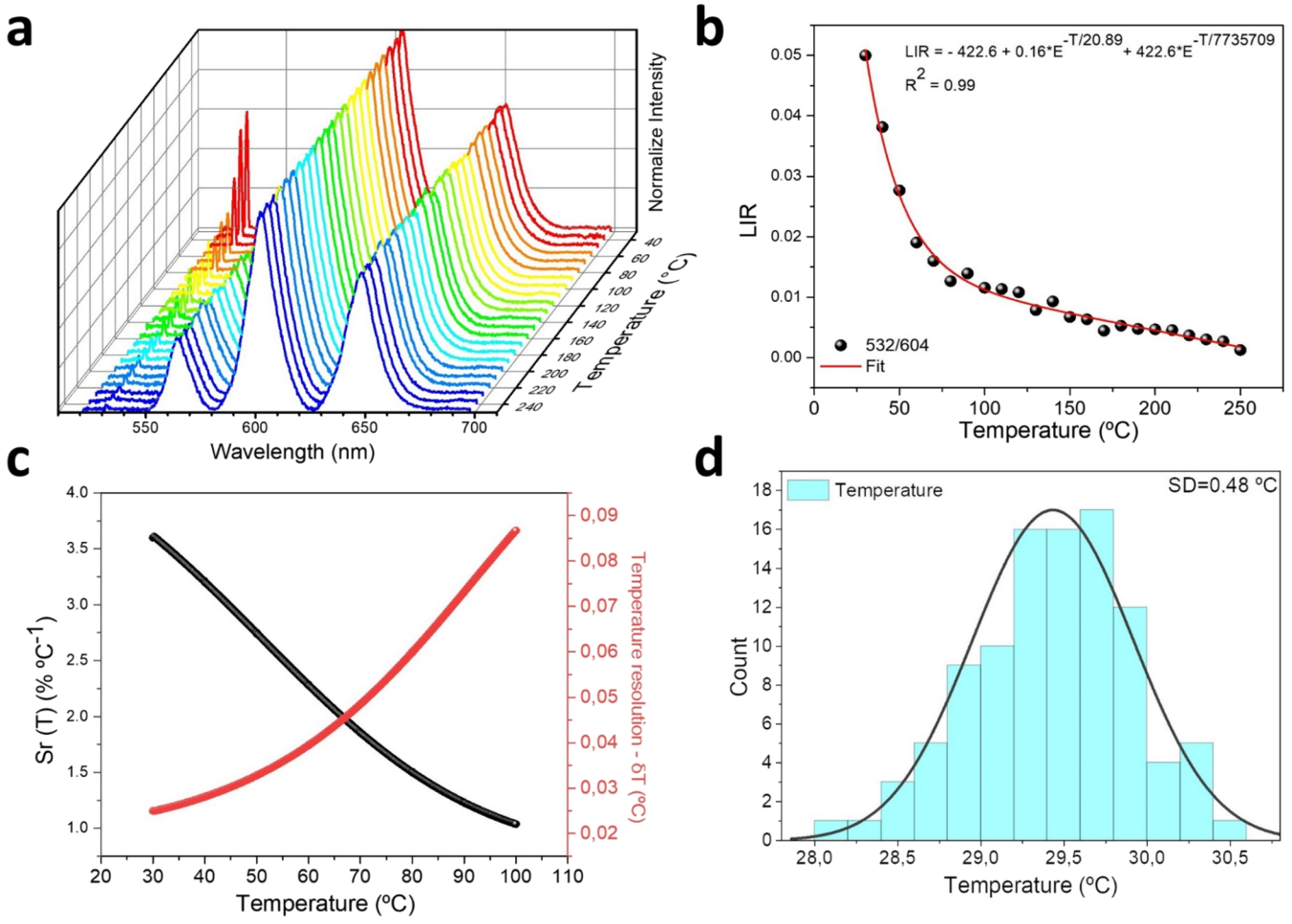

Figure 4. (a) Normalized emission spectra of Samarium and SGH of the sample as a function of temperature, measured using a double excitation with a continuous laser at 473 nm (≈0.6 KW·cm^{-2}) and a pulse laser at 1064 nm (≈1 W·cm^{-2}). (b) Determined band intensity ratios 532 nm/604 nm as a function of temperature. (c) Relative sensitivity and (d) temperature distribution obtained using 100 measurements in the same conditions at 30.0 °C.

elements inserted in Figure 2d. Figure 2e shows the high-resolution curve of Ti 2p. It has two spin−orbit split parts, Ti $2p_{3/2}$ and Ti $2p_{1/2}$, at 458.7 and 464.3 eV, generally considered to represent Ti^{4+}. Meanwhile, the peaks with lower binding energies (456.1 and 461.2 eV) correspond to the characteristic peaks associated with Ti^{3+}. The spin−orbit split parts of samarium $3d_{5/2}$ show a broad peak with three components, revealing the existence of more than one Sm ion (Figure 2f). The 1087 eV signal indicates the "2+" oxidation state of samarium, while the components at 1083.6 and 1085.1 eV confirm the existence of the "3+" oxidation state of samarium, in agreement with a previous report.[35]

To evaluate how the surface charge and size distribution behavior of PEG-coated BT:Sm NPs affect their transport efficiency and stability, the samples were dispersed across a wide pH range (3−10), as depicted in Figure 3.

Figure 3a,b shows that the results indicate that pH significantly affects the size distribution; mainly, it is observed that at the extremes of the pH range, attractive forces over repulsive ones promote the particle aggregation process. This result is attributable to the high ionic charge in the measurement conditions. On the other hand, in the pH values intermediate, it was observed that the aggregation reduced, showing size distribution with volume fraction under 200 nm for pH of 6, 7, and 8. In particular, at pH 7, the volume fraction reaches more than 50% by volume below 200 nm; this condition is favorable given that this is the size that ensures the biocompatibility of the NPs.[36,37] This observation aligns with the ζ potential measurements depicted in Figure 3c.

The zeta potential results corroborate the particle size distribution findings, indicating aggregation at extreme pH values due to the compression of the electrical double layer, which promotes van der Waals forces over electrostatic repulsion, leading to particle conglomerates. Conversely, at intermediate pH levels, a stable suspension of NPs is observed, with sizes conducive to biocompatibility testing. To ensure nanoparticle size is suitable for biocompatibility, ζ potential and size measurements were conducted using a continuous phase solution of standard Dulbecco's Modified Eagle's Medium (DMEM), with a pH range of 7.0−7.2, similar to the optimal stability condition observed in the pH sensitivity study. Results revealed a ζ potential of −37.4 mV and a volume fraction of 50% below 200 nm, indicating nanoparticle stability within the system.

3.2. Optical Properties of BT:Sm NPs. Figure 4a shows the dependence of the emission of the BT:Sm 5 mol % as a function of temperature under simultaneous excitation with a continuous laser at 473 nm (≈0.6 KW·cm^{-2}) and a pulsed laser at 1064 nm (≈ 1 W·cm^{-2}). Interestingly, the results were similar for all Sm^{3+}-doped samples, but the 5 mol % doped

https://doi.org/10.1021/acsomega.4c00974
ACS Omega 2024, 9, 28061−28071

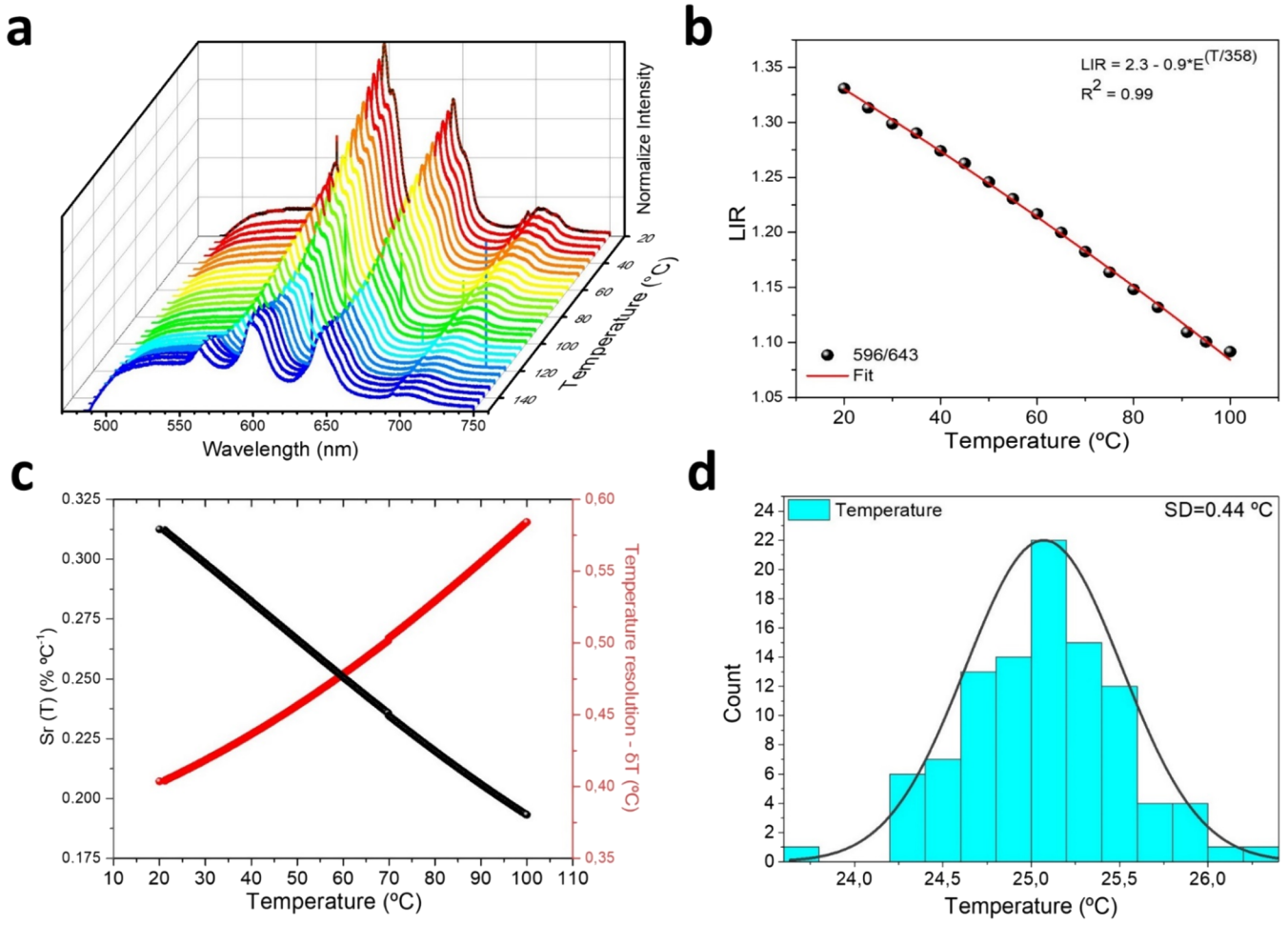

Figure 5. (a) DC emission spectra of the sample as a function of temperature, measured at λ_{ex} = 473 nm and ≈0.6 KW·cm^{-2}. (b) Determined band intensity ratios 596 nm/643 nm as a function of temperature. (c) Relative sensitivity and (d) temperature distribution were obtained using 100 measurements in the same conditions at 30.0 °C.

sample was selected because it shows a high emission intensity. Samarium emission bands shown in Figure 4a correspond with the transitions $^4G_{5/2} \rightarrow {}^6H_{5/2}$ (≈ 564 nm), $^4G_{5/2} \rightarrow {}^6H_{7/2}$ (≈ 604 nm), and $^4G_{5/2} \rightarrow {}^6H_{9/2}$ (≈ 643 nm); these emissions decrease smoothly with temperature, but the data are normalized using the peak at 604 nm. On the other hand, the peak at 532 nm corresponds to the second harmonic generation (SHG), whose intensity changes as the temperature increases. This allows us to develop a relationship using the following definition:

$$\mathrm{LIR} \equiv \frac{I_{532}}{I_{604}} \tag{1}$$

where the LIR is the luminescence intensity ratio between 532 and 604 nm emission bands shown in Figure 4b. With rising temperatures, there is a discernible decrease in the luminescence intensity ratio (LIR). This alteration in the LIR becomes particularly pronounced within lower temperature ranges (30−100 °C). This effect can be used for optical temperature sensors in biological applications.

To compare the performance of different sensors (so that the measurement configuration and the thermometric parameter used have no influence), it is useful to calculate their relative sensitivity (S_r) and the uncertainty (ΔT), given by the following formula:

$$S_r(T) = 100\% \times \frac{1}{\mathrm{LIR}} \frac{\mathrm{dLIR}}{\mathrm{d}T} \tag{2}$$

and

$$\delta T = \frac{1}{S_r} \frac{\delta \mathrm{LIR}}{\mathrm{LIR}} \tag{3}$$

where δLIR is the uncertainty of determination of the band intensity ratio 532 nm/604 nm. It is estimated from the LIR error using 100 measurements. Figure 4c shows how the LIR and Sr change within the temperature range of 30−100 °C. The relative sensitivity varies between 3.6 and 1% °C^{-1}, indicating good sensitivity.[38] To estimate the temperature uncertainty, 100 measurements were taken at 30 °C under the same conditions. As can be seen in Figure 4d, estimations of the 100 temperatures were made using the calibration equation shown in Figure 4b. This figure shows the distribution of the 100 temperatures, with a standard deviation of 0.48 °C.

Then, we perform a similar study but for the [(BT:Sm)-PEG] 5 mol % sample. Figure 5a shows the emission variation as a temperature function under simultaneous excitation with continuous laser at 473 nm (≈0.6 KW·cm^{-2}) and pulsed laser at 1064 nm (≈1 W·cm^{-2}). It is observed that the emission is a combination of the fluorescence of the organic coating plus the emission of the samarium and the SHG. However, the intensity of the SHG is negligible compared with the previous one. For

https://doi.org/10.1021/acsomega.4c00974
ACS Omega 2024, 9, 28061−28071

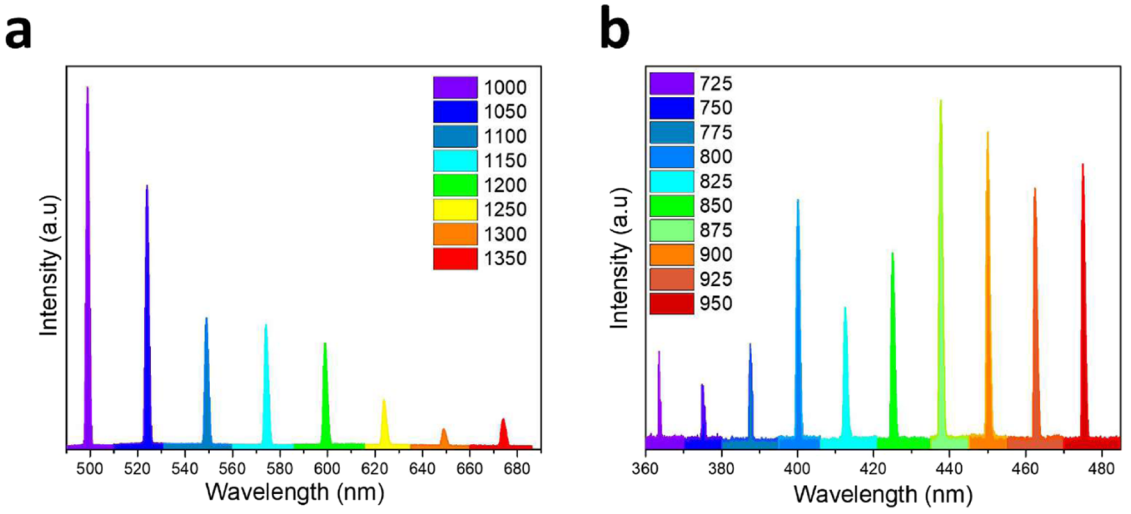

Figure 6. (a, b) SGH emission obtained using different excitation wavelengths for the BT:Sm 5 mol % NPs.

this reason, in this case, we reformulate the definition of the LIR used for the calculations:

$$\mathrm{LIR} \equiv \frac{I_{596}}{I_{643}} \tag{4}$$

where LIR is now defined as the luminescence ratio 596 nm ($^4G_{5/2} \rightarrow {}^6H_{7/2}$)/643 nm ($^4G_{5/2} \rightarrow {}^6H_{9/2}$), and the values are shown in Figure 5b. It is observed that when the temperature increases, the LIR decreases, so at 20 °C the LIR is 1.33, and at 100 °C it is 1.09. The relative sensitivity was calculated and is shown in Figure 5c. This parameter varies in the range of 20−100 °C. As in Figure 4d, 100 measurements were made, and the distribution of the temperatures is shown in Figure 5d. A similar standard deviation for the temperature values was obtained, indicating that these samples could be used to characterize the temperature.

As shown in Figures 4 and 5, the LIR method allows us to estimate the samples' temperature under laser excitation. Moreover, due to the characteristic of the SHG generation, it is interesting to note that in the BT:Sm 5 mol % sample, it is possible to change the excitation wavelength if necessary. Figure 6a,b illustrates the capability to generate SHG within the 360−680 nm range.

3.3. Cell Viability of Uncoated or PEG-Coated BT:Sm NPs. Developing new nanomaterials for use in biomedicine is one of the most promising applications of NPs. For this reason, studies have focused on biodegradable and biocompatible stabilizing agents for NPs.[39] PEG has been used as a stabilizing agent for NPs due to its availability, biocompatibility, and biodegradability.[40] To determine the biological effect of the synthesized NPs, we evaluated mitochondrial activity, as an indicator of cell viability, in cells exposed to uncoated or PEG-coated BT:Sm NPs using a WST-1 cell viability assay (Figure 6). The WST-1 assay is based on the cleavage of tetrazolium salt into formazan to measure the metabolic activity of mitochondria in living cells.[41] To achieve this, HEK293-T human cells were cultured with increasing concentrations of the Sm-doped NPs (0, 3, 6, 12, 50, 100, and 200 μg/mL), and the cleavage of tetrazolium salt was evaluated 24 h after NPs treatment.

The results illustrate that cells exposed to uncoated (black bars) or PEG-coated BT:Sm NPs (red bars) did not exhibit an alteration in mitochondrial activity (cell viability) (Figure 7). Regarding barium titanate (BT), these findings are consistent with studies examining uncoated BT-NP's biocompatibility. In human neuroblastoma (SHSY-5Y)[42] and pheochromocytoma (PC-12) cells,[43] no significant decrease in cell viability has been reported when using BT-NPs. In addition, another study reported the effect of uncoated BT-NPs on cancerous and noncancerous cell lines, where the NPs did not exhibit a cytotoxic effect on noncancerous human lung fibroblasts (IMR-90).[44] However, BT-NPs decreased cancerous A549 cell viability in a dose- and time-dependent manner,[44] as has also been reported for breast cancer cell MCF-7.[45] Similar studies of biological compatibility in cell cultures have been performed using other nanocomposites. Basouri et al. show the anticancer effect of Ag-doped MgO-NiO-ZnO nanocomposite on normal L929 and cancer B16F0 cell lines.[46] The authors did not show any lethal effect on normal L929 cells, but they reported cytotoxic effects in cancer cells, according to the result of the MTT cell viability assay. The same results of the anticancer effect were obtained on mouse melanoma B16F0 cell lines after 48 h.[47] Finally, this group studied the cytotoxicity of cinnamon NPs. At higher concentrations, toxic effects were reported in human liver cancer HepG2 cells.[48] In concordance with these results, we have not evidenced changes in cell viability in noncancerous human embryonic kidney cells (HEK293-T).

NPs are being investigated in the context of biological compatibility for use as contrast agents.[49] Moreover, theranostic applications can be developed by combining therapeutic and diagnostic enhancements in the same NPs. For example, the Au NPs can improve computed tomography (CT) contrast with enhanced X-ray attenuation compared to surrounding tissues and therapeutic capability.[50,51] The radiosensitizing effects of TiO_2 NPs can be enhanced by incorporating other high Z elements into these NPs while preserving their basic properties. For this reason, we incorporated Sm into these NPs to enhance their radiosensitizing effects and synthesized BT-NPs doped with different amounts of Sm. In Figure 7, no significant differences are observed in the viability of cells exposed to doped BT:Sm NPs. (Figure 7a−c). This fact is supported by another study in which Sm was used as a doping agent in TiO_2 NPs. This study observed no alterations in cellular uptake and cell viability were

https://doi.org/10.1021/acsomega.4c00974
ACS Omega 2024, 9, 28061−28071

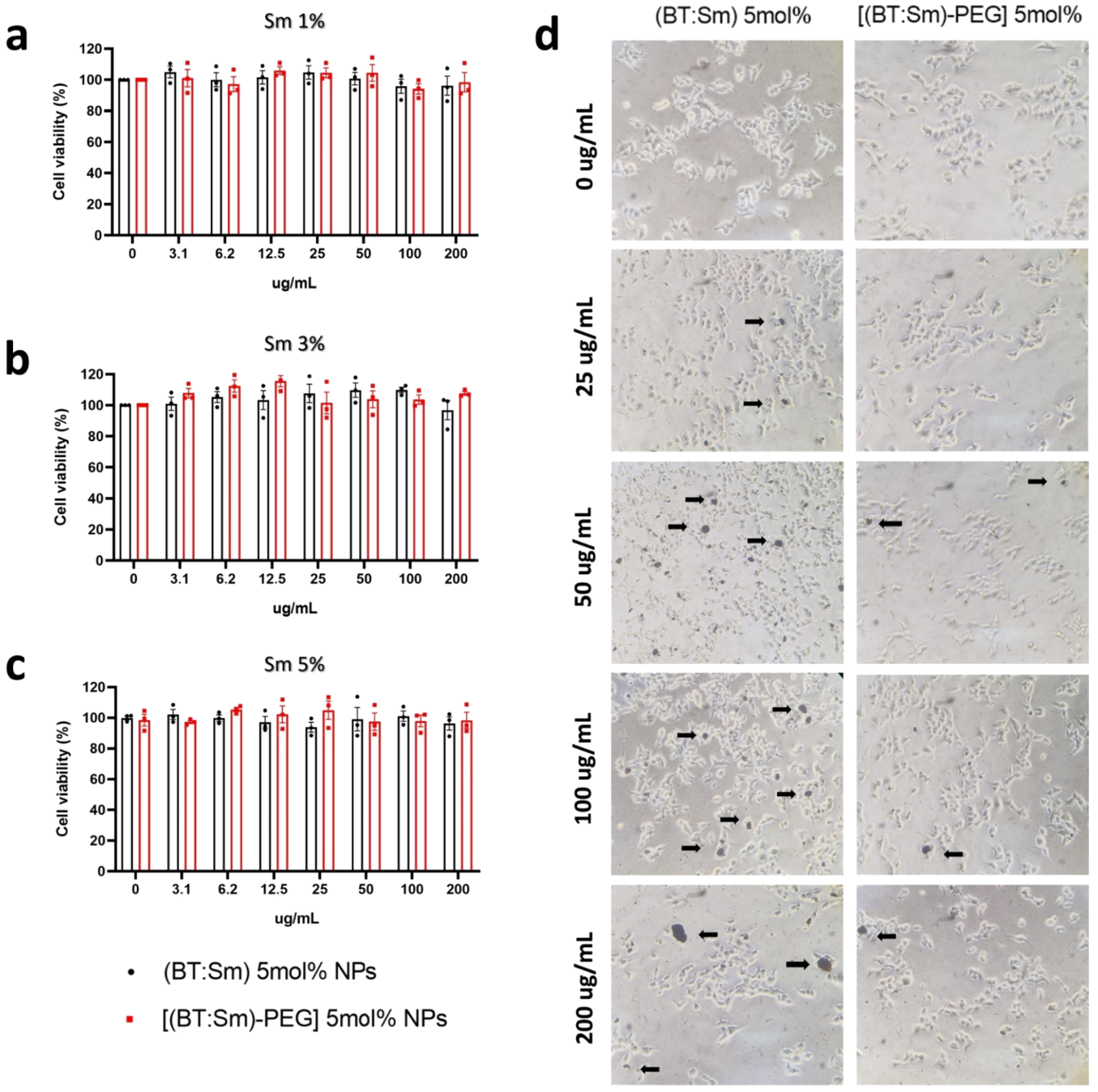

Figure 7. Effect of naked and PEG-coated BT:Sm NPs on the cell viability of HEK293-T cells. Data represent mean ± SEM of viable cells (as a percentage of control; 0 μg/mL) treated 24 h with naked (black bars) or PEG-coated BT:Sm NPs (red bars) doped with (a) Sm 1, (b) Sm 3, and (c) Sm 5 mol %. (d) Representative images of HEK293-T cells exposed to different concentrations of naked and PEG-coated BT:Sm 5 mol %.

observed with Sm doping.[52] Therefore, Sm is compatible and can be used as a doping agent for BT-NPs.

In addition, we performed a qualitative examination through phase-contrast microscopy to validate the colorimetric cell viability assay, WST-1. The cellular morphology was examined following a 24 h exposure to BT:Sm NPs, as depicted in Figure 7d. The HEK293-T cells not exposed to NPs during the visual assessment demonstrated normal and healthy shape. HEK293-T cells were treated with varying concentrations of uncoated and PEG-coated BT:Sm NPs, and the NPs were subjected to sonication before incubation with the cells. The microscopy visualization showed that the cellular morphology observed was comparable to that of the control group. As anticipated, BT:Sm NPs demonstrated heterogeneous levels of aggregation (Figure 7d, shown by black arrows), as previously reported by others.[53−55] The black dots are higher in cells subjected to uncoated BT:Sm NPs than in cells treated with (PEG)-coated BT:Sm NPs. Consequently, the incorporation of PEG would enhance the solubility of these NPs in physiological fluids.

Maintaining NPs with high levels of stability and uniformity is crucial. However, aggregation poses a significant challenge that often undermines the stability and efficacy of nanocarriers.[56] Furthermore, the impact of this intricate biological fluid on the colloidal properties of NPs must be addressed more fully. The impact of alterations in the dispersion state of NPs on future cellular contact and response has been

https://doi.org/10.1021/acsomega.4c00974
ACS Omega 2024, 9, 28061−28071

demonstrated, highlighting the significance of investigating this matter.[57,58] Future studies will enable us to understand the effect of the chemical composition of NPs on their functional characteristics. Thus, the results support the idea that poly(ethylene glycol) (PEG)-coated BT:Sm NPs are compatible with biological entities.

4. CONCLUSIONS

In conclusion, the simultaneous integration of SHG and MP-PL in poly(ethylene glycol) (PEG)-coated BT:Sm NPs can potentially advance nonlinear optics and biophotonics significantly. Also, we showed that coating BT:Sm NPs with PEG shows compatibility with biological systems. Moreover, it has been shown that under laser excitation and using the luminescence intensity ratio of two bands, these nanoparticles can be used to determine the temperature with a resolution better than 0.5 °C. This study illuminates the fundamental mechanisms governing the optical behavior of these multifunctional nanoparticles and demonstrates their suitability for various applications. Future research can concentrate on optimizing the properties of these nanoparticles and investigating their potential for the creation of advanced optical devices and biophotonic technologies.

AUTHOR INFORMATION

Corresponding Authors

Sandra Fuentes − *Departamento de Ciencias Farmacéuticas, Facultad de Ciencias, Universidad Católica del Norte, 1280 Antofagasta, Chile; Center for the Development of Nanoscience and Nanotechnology, CEDENNA, Santiago 9160000, Chile;* orcid.org/0000-0001-6977-1610; Email: sfuentes@ucn.cl

Inocencio R. Martín − *Departamento de Física, MALTA-Consolider Team, IMN, Universidad de La Laguna, E-38206 San Cristóbal de La Laguna, Santa Cruz de Tenerife, Spain*; Email: imartin@ull.edu.es

Authors

Duxan Arancibia − *Departamento de Ciencias Farmacéuticas, Facultad de Ciencias, Universidad Católica del Norte, 1280 Antofagasta, Chile*

Marcelo Rojas − *Departamento de Ciencias Farmacéuticas, Facultad de Ciencias, Universidad Católica del Norte, 1280 Antofagasta, Chile*

Francisca Carmona − *Departamento de Ciencias Farmacéuticas, Facultad de Ciencias, Universidad Católica del Norte, 1280 Antofagasta, Chile*

Andrea Ortega − *Departamento de Procesos Diagnósticos y Evaluación, Facultad de Ciencias de la Salud, Universidad Católica de Temuco, Temuco 4813302 La Araucanía, Chile*

Julio Valenzuela − *Departamento de Minas y Metalurgia, Universidad Católica del Norte, Antofagasta 1280, Chile*

Christian Hernández-Álvarez − *Departamento de Física, MALTA-Consolider Team, IMN, Universidad de La Laguna, E-38206 San Cristóbal de La Laguna, Santa Cruz de Tenerife, Spain*

Complete contact information is available at: https://pubs.acs.org/10.1021/acsomega.4c00974

Notes

The authors declare no competing financial interest.

ACKNOWLEDGMENTS

This work has been partially financed by P. Fondecyt 1190721. S.F. thanks to FONDEQUIP project EQM140044, Scientific Equipment Unit − MAINI of Universidad Católica del Norte and Basal Financing Program CONICYT, AFB220001 (CEDENNA).

REFERENCES

(1) Sajja, H. K.; East, M. P.; Mao, H.; Wang, A. Y.; Nie, S.; Yang, L. Development of Multifunctional Nanoparticles for Targeted Drug Delivery and Non-Invasive Imaging of Therapeutic Effect. *Curr. Drug Discovery Technol.* **2009**, *6* (1), 43−51.

(2) Sood, A.; Desseigne, M.; Dev, A.; Maurizi, L.; Kumar, A.; Millot, N.; Han, S. S. A Comprehensive Review on Barium Titanate Nanoparticles as a Persuasive Piezoelectric Material for Biomedical Applications: Prospects and Challenges. *Small* **2023**, *19* (12), No. 2206401.

(3) Hsieh, C.-L.; Grange, R.; Pu, Y.; Psaltis, D. Bioconjugation of Barium Titanate Nanocrystals with Immunoglobulin G Antibody for Second Harmonic Radiation Imaging Probes. *Biomaterials* **2010**, *31* (8), 2272−2277.

(4) Kim, E.; Steinbrück, A.; Buscaglia, M. T.; Buscaglia, V.; Pertsch, T.; Grange, R. Second-Harmonic Generation of Single BaTiO3 Nanoparticles down to 22 Nm Diameter. *ACS Nano* **2013**, *7* (6), 5343−5349.

(5) Frizyuk, K. S.; Smirnova, D. A.; Poddubny, A. N.; Petrov, M. I. Second Harmonic Generation in Nanoparticles with Mie Resonances. *J. Phys.: Conf. Ser.* **2018**, *1092* (1), No. 012037.

(6) Bijeesh, M. M.; Shakhi, P. K.; Arunkarthick, S.; Varier, G. K.; Nandakumar, P. Confocal Imaging of Single BaTiO3 Nanoparticles by Two-Photon Photothermal Microscopy. *Sci. Rep.* **2017**, *7*, No. 1643, DOI: 10.1038/s41598-017-01548-z.

(7) Acharyya, J. N.; Desai, N. R.; Gangineni, R. B.; Prakash, G. V. Photonic Cavity-Mediated Tunable Ultrafast Absorption Dynamics in BaTiO3-Based One-Dimensional Photonic Crystal. *ACS Appl. Electron. Mater.* **2021**, *3* (4), 1904−1911.

(8) Yang, Y.; Tu, D.; Zhang, Y.; Zhang, P.; Chen, X. Recent Advances in Design of Lanthanide-Containing NIR-II Luminescent Nanoprobes. *iScience* **2021**, *24* (2), No. 102062.

(9) Tu, D.; Liu, Y.; Zhu, H.; Li, R.; Liu, L.; Chen, X. Breakdown of Crystallographic Site Symmetry in Lanthanide-Doped NaYF4 Crystals. *Angew. Chem., Int. Ed. Engl.* **2013**, *52* (4), 1128−1133.

(10) V.Barbosa, I.; Maia, L. J. Q.; Ibanez, A.; Dantelle, G. Recent Developments on BW-II and BW-III Ratiometric Luminescent Nanothermometers for in Vivo Thermal Sensing. *Opt. Mater.: X* **2023**, *18*, No. 100236.

(11) Xu, J.; Gulzar, A.; Yang, P.; Bi, H.; Yang, D.; Gai, S.; He, F.; Lin, J.; Xing, B.; Jin, D. Recent Advances in Near-Infrared Emitting Lanthanide-Doped Nanoconstructs: Mechanism, Design and Application for Bioimaging. *Coord. Chem. Rev.* **2019**, *381*, 104−134.

(12) Smith, A. M.; Mancini, M. C.; Nie, S. Bioimaging: Second Window for in Vivo Imaging. *Nat. Nanotechnol.* **2009**, *4* (11), 710−711.

(13) Li, Y.; Zeng, S.; Hao, J. Non-Invasive Optical Guided Tumor Metastasis/Vessel Imaging by Using Lanthanide Nanoprobe with Enhanced Down-Shifting Emission beyond 1500 Nm. *ACS Nano* **2019**, *13* (1), 248−259.

(14) Zhong, Y.; Ma, Z.; Zhu, S.; Yue, J.; Zhang, M.; Antaris, A. L.; Yuan, J.; Cui, R.; Wan, H.; Zhou, Y.; Wang, W.; Huang, N. F.; Luo, J.; Hu, Z.; Dai, H. Boosting the Down-Shifting Luminescence of Rare-Earth Nanocrystals for Biological Imaging beyond 1500 Nm. *Nat. Commun.* **2017**, *8* (1), No. 737, DOI: 10.1038/s41467-017-00917-6.

(15) Bai, J.-W.; Qiu, S.-Q.; Zhang, G.-J. Molecular and Functional Imaging in Cancer-Targeted Therapy: Current Applications and Future Directions. *Signal Transduction Targeted Ther.* **2023**, *8* (1), 1−32.

(16) McNamara, K.; Tofail, S. A. M. Nanoparticles in Biomedical Applications. *Adv. Phys.: X* **2017**, *2* (1), 54−88.

(17) Thanh, N. T. K.; Green, L. A. W. Functionalisation of Nanoparticles for Biomedical Applications. *Nano Today* **2010**, *5* (3), 213−230.
(18) Suk, J. S.; Xu, Q.; Kim, N.; Hanes, J.; Ensign, L. M. PEGylation as a Strategy for Improving Nanoparticle-Based Drug and Gene Delivery. *Adv. Drug Delivery Rev.* **2016**, *99* (Pt A), 28−51.
(19) Mishra, P.; Nayak, B.; Dey, R. K. PEGylation in Anti-Cancer Therapy: An Overview. *Asian J. Pharm. Sci.* **2016**, *11* (3), 337−348.
(20) Huang, R. H.; Sobol, N. B.; Younes, A.; Mamun, T.; Lewis, J. S.; Ulijn, R. V.; O'Brien, S. Comparison of Methods for Surface Modification of Barium Titanate Nanoparticles for Aqueous Dispersibility: Towards Biomedical Utilization of Perovskite Oxides. *ACS Appl. Mater. Interfaces* **2020**, *12* (46), 51135−51147.
(21) Jokerst, J. V.; Lobovkina, T.; Zare, R. N.; Gambhir, S. S. Nanoparticle PEGylation for Imaging and Therapy. *Nanomedicine* **2011**, *6* (4), 715−728.
(22) D'souza, A. A.; Shegokar, R. Polyethylene Glycol (PEG): A Versatile Polymer for Pharmaceutical Applications. *Expert Opin. Drug Delivery* **2016**, *13* (9), 1257−1275.
(23) Shi, L.; Zhang, J.; Zhao, M.; Tang, S.; Cheng, X.; Zhang, W.; Li, W.; Liu, X.; Peng, H.; Wang, Q. Effects of Polyethylene Glycol on the Surface of Nanoparticles for Targeted Drug Delivery. *Nanoscale* **2021**, *13* (24), 10748−10764.
(24) Hoang Thi, T. T.; Pilkington, E. H.; Nguyen, D. H.; Lee, J. S.; Park, K. D.; Truong, N. P. The Importance of Poly(Ethylene Glycol) Alternatives for Overcoming PEG Immunogenicity in Drug Delivery and Bioconjugation. *Polymers* **2020**, *12* (2), 298.
(25) Dabagh, S.; Haris, S. A.; Ertas, Y. N. Engineered Polyethylene Glycol-Coated Zinc Ferrite Nanoparticles as a Novel Magnetic Resonance Imaging Contrast Agent. *ACS Biomater. Sci. Eng.* **2023**, *9* (7), 4138−4148.
(26) Sun, S.; Cui, Y.; Yuan, B.; Dou, M.; Wang, G.; Xu, H.; Wang, J.; Yin, W.; Wu, D.; Peng, C. Drug Delivery Systems Based on Polyethylene Glycol Hydrogels for Enhanced Bone Regeneration. *Front. Bioeng. Biotechnol.* **2023**, *11*, No. 1117647, DOI: 10.3389/fbioe.2023.1117647.
(27) Hillegass, J. M.; Shukla, A.; Lathrop, S. A.; MacPherson, M. B.; Fukagawa, N. K.; Mossman, B. T. Assessing Nanotoxicity in Cells in Vitro. *Wiley Interdiscip. Rev.: Nanomed. Nanobiotechnol.* **2010**, *2* (3), 219−231.
(28) Krpetić, Z.; Anguissola, S.; Garry, D.; Kelly, P. M.; Dawson, K. A. Nanomaterials: Impact on Cells and Cell Organelles. *Adv. Exp. Med. Biol.* **2014**, *811*, 135−156.
(29) Foroozandeh, P.; Aziz, A. A. Insight into Cellular Uptake and Intracellular Trafficking of Nanoparticles. *Nanoscale Res. Lett.* **2018**, *13* (1), 339.
(30) Fuentes, S.; Pizarro, H.; Gutiérrez, P.; Diaz-Droguett, D. E.; Barraza, N. Application of FORC Distributions to the Study of Magnetic Interactions in Co-Doped BaTiO3 Nanomaterials. *Mater. Sci. Eng.: B* **2018**, *227*, 39−47.
(31) Fuentes, S.; Céspedes, F.; Muñoz, P.; Chavez, E.; Padilla-Campos, L. SYNTHESIS AND STRUCTURAL CHARACTERIZATION OF NANOCRYSTALLINE BATIO3 AT VARIOUS CALCINATION TEMPERATURES. *J. Chil. Chem. Soc.* **2013**, *58* (4), 2077−2081.
(32) Cheraghali, S.; Dini, G.; Caligiuri, I.; Back, M.; Rizzolio, F. PEG-Coated MnZn Ferrite Nanoparticles with Hierarchical Structure as MRI Contrast Agent. *Nanomaterials* **2023**, *13* (3), 452.
(33) Kumar, S.; Luthra, V. Raman and Infrared Spectroscopic Investigation of the Effects of Yttrium and Tin Co-Doping in Barium Titanate. *J. Phys. Chem. Solids* **2021**, *154*, No. 110079.
(34) Busca, G.; Buscaglia, V.; Leoni, M.; Nanni, P. Solid-State and Surface Spectroscopic Characterization of BaTiO3 Fine Powders. *Chem. Mater.* **1994**, *6* (7), 955−961.
(35) Leote, R. J. B.; Matei, E.; Apostol, N. G.; Enculescu, M.; Enculescu, I.; Diculescu, V. C. Monodispersed Nanoplatelets of Samarium Oxides for Biosensing Applications in Biological Fluids. *Electrochim. Acta* **2022**, *402*, No. 139532.
(36) Harish, V.; Ansari, M. M.; Tewari, D.; Yadav, A. B.; Sharma, N.; Bawarig, S.; García-Betancourt, M.-L.; Karatutlu, A.; Bechelany, M.; Barhoum, A. Cutting-Edge Advances in Tailoring Size, Shape, and Functionality of Nanoparticles and Nanostructures: A Review. *J. Taiwan Inst. Chem. Eng.* **2023**, *149*, No. 105010.
(37) Yadav, S.; Chamoli, S.; Kumar, P.; Maurya, P. K. Structural and Functional Insights in Polysaccharides Coated Cerium Oxide Nanoparticles and Their Potential Biomedical Applications: A Review. *Int. J. Biol. Macromol.* **2023**, *246*, No. 125673.
(38) Brites, C. D. S.; Millán, A.; Carlos, L. D. Lanthanides in Luminescent Thermometry. In *Including Actinides*; Elsevier, 2016; Vol. *49*, pp 339−427 DOI: 10.1016/bs.hpcre.2016.03.005.
(39) Javed, R.; Zia, M.; Naz, S.; Aisida, S. O.; Ain, N. U.; Ao, Q. Role of Capping Agents in the Application of Nanoparticles in Biomedicine and Environmental Remediation: Recent Trends and Future Prospects. *J. Nanobiotechnol.* **2020**, *18* (1), 172.
(40) Boisselier, E.; Astruc, D. Gold Nanoparticles in Nanomedicine: Preparations, Imaging, Diagnostics, Therapies and Toxicity. *Chem. Soc. Rev.* **2009**, *38* (6), 1759−1782.
(41) Ngamwongsatit, P.; Banada, P. P.; Panbangred, W.; Bhunia, A. K. WST-1-Based Cell Cytotoxicity Assay as a Substitute for MTT-Based Assay for Rapid Detection of Toxigenic Bacillus Species Using CHO Cell Line. *J. Microbiol. Methods* **2008**, *73* (3), 211−215.
(42) Ciofani, G.; Danti, S.; D'Alessandro, D.; Moscato, S.; Petrini, M.; Menciassi, A. Barium Titanate Nanoparticles: Highly Cytocompatible Dispersions in Glycol-Chitosan and Doxorubicin Complexes for Cancer Therapy. *Nanoscale Res. Lett.* **2010**, *5* (7), 1093−1101.
(43) Candito, M.; Simoni, E.; Gentilin, E.; Martini, A.; Marioni, G.; Danti, S.; Astolfi, L. Neuron Compatibility and Antioxidant Activity of Barium Titanate and Lithium Niobate Nanoparticles. *Int. J. Mol. Sci.* **2022**, *23* (3), 1761.
(44) Ahamed, M.; Akhtar, M. J.; Khan, M. M.; Alhadlaq, H. A.; Alshamsan, A. Barium Titanate (BaTiO3) Nanoparticles Exert Cytotoxicity through Oxidative Stress in Human Lung Carcinoma (A549) Cells. *Nanomaterials* **2020**, *10* (11), 2309.
(45) Fakhar-e-Alam, M.; Saddique, S.; Hossain, N.; Shahzad, A.; Ullah, I.; Sohail, A.; Khan, M. J. I.; Saadullah, M. Synthesis, Characterization, and Application of BaTiO3 Nanoparticles for Anti-Cancer Activity. *J. Cluster Sci.* **2023**, *34* (4), 1745−1755.
(46) Sabouri, Z.; Kazemi, M.; Sabouri, M.; Moghaddas, S. S. T. H.; Darroudi, M. Biosynthesis of Ag Doped MgO-NiO-ZnO Nanocomposite with *Ocimum Basilicum L* Extract and Assessment of Their Biological and Photocatalytic Applications. *J. Mol. Struct.* **2024**, *1306*, No. 137895, DOI: 10.1016/j.molstruc.2024.137895.
(47) Sabouri, Z.; Sammak, S.; Sabouri, S.; Moghaddas, S. S. T. H.; Darroudi, M. Green Synthesis of Ag-Se Doped ZnO-Co3O4-NiO Fivenary Nanocomposite Using Poly Anionic Cellulose and Evaluation of Their Anticancer and Photocatalyst Applications. *Chem. Methodol.* **2024**, *8* (3), 164−176, DOI: 10.48309/chemm.2024.436507.1758.
(48) Sabouri, Z.; Shakour, N.; Sabouri, M.; Moghaddas, S. S. T. H.; Darroudi, M. Biochemical, Structural Characterization and Assessing the Biological Effects of Cinnamon Nanoparticles. *Biotechnol. Bioprocess. Eng.* **2024**, *29* (1), 165−175, DOI: 10.1007/s12257-024-00004-w.
(49) Wang, A. Z.; Tepper, J. E. Nanotechnology in Radiation Oncology. *J. Clin. Oncol.* **2014**, *32* (26), 2879−2885.
(50) Jackson, P. A.; Rahman, W. N. W. A.; Wong, C. J.; Ackerly, T.; Geso, M. Potential Dependent Superiority of Gold Nanoparticles in Comparison to Iodinated Contrast Agents. *Eur. J. Radiol.* **2010**, *75* (1), 104−109.
(51) Dong, Y. C.; Hajfathalian, M.; Maidment, P. S. N.; Hsu, J. C.; Naha, P. C.; Si-Mohamed, S.; Breuilly, M.; Kim, J.; Chhour, P.; Douek, P.; Litt, H. I.; Cormode, D. P. Effect of Gold Nanoparticle Size on Their Properties as Contrast Agents for Computed Tomography. *Sci. Rep.* **2019**, *9* (1), No. 14912, DOI: 10.1038/s41598-019-50332-8.
(52) Nakayama, M.; Smith, C. L.; Feltis, B. N.; Piva, T. J.; Tabatabaie, F.; Harty, P. D.; Gagliardi, F. M.; Platts, K.; Otto, S.;

Blencowe, A.; Morita, K.; Geso, M. Samarium Doped Titanium Dioxide Nanoparticles as Theranostic Agents in Radiation Therapy. *Phys. Med.* **2020**, *75*, 69−76.
(53) Zhao, J.; Wang, X.; Chen, R.; Li, L. Dispersion of Barium Titanate in Aqueous Media. *Ceram. Int.* **2007**, *33* (2), 207−212.
(54) Kim, P.; Doss, N. M.; Tillotson, J. P.; Zhang, X.-H.; Jones, S. C.; Hotchkiss, P. J.; Li, J.; Calame, J. P.; Domercq, B.; Kippelen, B.; Marder, S. R.; Perry, J. W. High Performance Polymer/BaTiO3 Nanocomposites Based on Surface-Modified Metal Oxide Nanoparticles Using Functional Phosphonic Acids for Electronic Applications. *MRS Online Proc. Libr.* **2008**, *1113* (1), 205.
(55) Hu, P.; Gao, S.; Zhang, Y.; Zhang, L.; Wang, C. Surface Modified BaTiO3 Nanoparticles by Titanate Coupling Agent Induce Significantly Enhanced Breakdown Strength and Larger Energy Density in PVDF Nanocomposite. *Compos. Sci. Technol.* **2018**, *156*, 109−116.
(56) Shrestha, S.; Wang, B.; Dutta, P. Nanoparticle Processing: Understanding and Controlling Aggregation. *Adv. Colloid Interface Sci.* **2020**, *279*, No. 102162.
(57) Albanese, A.; Chan, W. C. Effect of Gold Nanoparticle Aggregation on Cell Uptake and Toxicity. *ACS Nano* **2011**, *5* (7), 5478−5489.
(58) Hirsch, V.; Salaklang, J.; Rothen-Rutishauser, B.; Petri-Fink, A. Influence of Serum Supplemented Cell Culture Medium on Colloidal Stability of Polymer Coated Iron Oxide and Polystyrene Nanoparticles with Impact on Cell Interactions in Vitro. *IEEE Trans. Magn.* **2013**, *49* (1), 402−407.

https://doi.org/10.1021/acsomega.4c00974
ACS Omega 2024, 9, 28061−28071